

# XCO<sub>2</sub> in an emission hot-spot region: the COCCON Paris campaign 2015

F.R. Vogel<sup>1,a</sup>, M. Frey<sup>2</sup>, J. Stauffer<sup>3,a</sup>, F. Hase<sup>2</sup>, G. Broquet<sup>4</sup>, I. Xueref-Remy<sup>5,a</sup>, F. Chevallier<sup>4</sup>, P. Ciais<sup>4</sup>, M. K. Sha<sup>6,b</sup>, P. Chelin<sup>7</sup>, P. Jeseck<sup>8</sup>, C. Janssen, Y. V. Te<sup>8</sup>, J. Groß<sup>2</sup>, T. Blumenstock<sup>2</sup>, Q. Tu<sup>2</sup> and J. Orphal<sup>2</sup>

1. Climate Research Division, Environment and Climate Change Canada, Toronto, Canada

2. Karlsruhe Institute of Technology (KIT), Institute of Meteorology and Climate Research (IMK), Karlsruhe, Germany

3. Thales, Labège, France

4. Laboratoire des Sciences du Climat et de l'Environnement (LSCE), IPSL, CEA-CNRS-UVSQ, Université Paris-Saclay, Gif-Sur-Yvette, France

5. Observatoire de Haute Provence, OSU Pytheas, Saint-Michel l'Observatoire, France

6. Royal Belgian Institute for Space Aeronomy, Brussels, Belgium

7. Laboratoire Inter-Universitaire des Systèmes Atmosphériques (LISA), (CNRS UMR 7583, Université Paris Est Créteil, Université Paris Diderot, Institut Pierre Simon Laplace), Créteil, France.

8. Laboratoire d'Études du Rayonnement et de la Matière en Astrophysique et Atmosphères (LERMA), IPSL, Sorbonne Universités, (CNRS, PSL Research University, Observatoire de Paris), Paris, France

Previously at

a. Laboratoire des Sciences du Climat et de l'Environnement (LSCE), IPSL, CEA-CNRS-UVSQ, Université Paris-Saclay, Gif-Sur-Yvette, France

b. Karlsruhe Institute of Technology (KIT), Institute of Meteorology and Climate Research (IMK), Karlsruhe, Germany

*Correspondence to: Felix R. Vogel (Felix.Vogel@canada.ca)*

**Abstract.** Providing timely information on urban Greenhouse-Gas (GHG) emissions and their trends to stakeholders relies on reliable measurements of atmospheric concentrations and the understanding of how local emissions and atmospheric transport influence these observations.

Portable Fourier Transform Infra-Red (FTIR) spectrometers were deployed at 5 stations in the Paris metropolitan area to provide column-averaged concentrations of CO<sub>2</sub> (XCO<sub>2</sub>) during a field campaign in spring of 2015, as part of the Collaborative Carbon Column Observing Network (COCCON). Here, we describe and analyze the variations of XCO<sub>2</sub> observed at

different sites and how they changed over time. We find that observations upwind and downwind of the city centre differ significantly in their XCO<sub>2</sub> concentrations, while the overall variability of the daily cycle is similar, i.e., increasing during night-time with a strong decrease (typically 2-3 ppm) during the afternoon.

An atmospheric transport model framework (CHIMERE-CAMS) was used to simulate XCO<sub>2</sub> and predict the same behaviour seen in the observations, which supports key findings, e.g. that even in a densely populated region like Paris (over 12 Million people), biospheric uptake of CO<sub>2</sub> can be of major influence on daily XCO<sub>2</sub> variations. Despite a general offset between modelled and observed XCO<sub>2</sub>, the model correctly predicts the impact of the meteorological parameters (e.g. wind direction and speed) on the concentration gradients between different stations. When analysing local gradients of XCO<sub>2</sub> for upwind and downwind station pairs, those found to be less sensitive to changes in XCO<sub>2</sub> boundary conditions and biogenic fluxes within the domain and we find the model-data agreement further improves. Our modelling framework indicates that the local XCO<sub>2</sub> gradient between the stations is dominated by the fossil fuel CO<sub>2</sub> signal of the Paris metropolitan area. This further highlights the potential usefulness of XCO<sub>2</sub> observations to help optimise future urban GHG emission estimates.

## 1 Introduction

Atmospheric background concentrations of CO<sub>2</sub> measured since 1958 in Mauna Loa, USA, have passed the symbolic milestone of 400 ppm (monthly mean) as of 2013 [Jones 2013]. Properly quantifying fossil fuel CO<sub>2</sub> emissions (FFCO<sub>2</sub>) can contribute to define effective climate mitigation strategies. Focussing our attention on cities is a critical part of this endeavour as emissions from urban areas are currently estimated to represent from 53 % to 87 % of global FFCO<sub>2</sub>, depending on the accounting method considered, and are predicted to increase further [IPCC-WG3 2014, IEA 2008, Dhakal 2009]. As stated in the IPCC 5<sup>th</sup> assessment report, “*current and future urbanisations trends are significantly different from the past*” and “*no single factor explains variations in per-capita emissions across cities and there are significant differences in per capita greenhouse gas (GHG) emissions between cities within a single country*” [IPCC-WG3 2014]. Therefore, findings in one city can often not be simply extrapolated to other urban regions. Furthermore, the large uncertainty of the global contribution of urban areas to CO<sub>2</sub> emissions today and in the future is why a new generation of city-scale observing and modelling systems are needed.

In recent years, more and more atmospheric networks have emerged that observe GHG concentrations using the atmosphere as a large-scale integrator, for example in Paris, France (e.g., Bréon et al. 2015, Xueref-Remy et al, 2018), Indianapolis, USA (e.g. Turnbull et al. 2015, Lauvaux et al. 2016), Salt Lake City, USA (Strong et al. 2011, Mitchell et al. 2018), Heidelberg, Germany (e.g. Levin et al. 2011, Vogel et al. 2013) and Toronto, Canada (e.g. Vogel et al.

2012). The air measured at in-situ ground-based stations is considered to be representative of surface CO<sub>2</sub> fluxes of a larger surrounding area (1 km<sup>2</sup>-10000 km<sup>2</sup>), i.e. the emissions of the Greater Paris Area dominate the airshed of the Ile-de-France (ca. 12000 km<sup>2</sup>) (Stauffer et al. 2016). If CO<sub>2</sub> measurements are performed both up-wind and downwind of a city, the concentration gradient between the two locations is influenced by the local net flux strength between both sites and atmospheric mixing [Xueref-Remy et al, 2018, Bréon et al. 2015, Turnbull et al. 2015]. To derive quantitative flux estimates, measured concentration data are typically assimilated into numerical atmospheric transport models which calculate the impact of atmospheric mixing on concentration gradients for a given flux space-time distribution. Such a data assimilation framework implemented for Paris with three atmospheric CO<sub>2</sub> measurement sites [Xueref-Remy et al, 2018] previously allowed deriving quantitative estimates of monthly emissions and their uncertainties over one year [Stauffer et al. 2016].

Space-borne measurements of the column-average dry air mole fraction of CO<sub>2</sub> (XCO<sub>2</sub>) are increasingly considered for the monitoring of urban CO<sub>2</sub>. This potential was shown with OCO-2 and GOSAT XCO<sub>2</sub> measurements, even though the spatial coverage and temporal sampling frequency of these two instruments were not optimized for FFCO<sub>2</sub> [Kort et al., 2012, Janardanan et al. 2016, Schwandner et al. 2017], while other space-borne sensors dedicated to FFCO<sub>2</sub> and with an imaging capability are in preparation [O'Brien et al, 2016, Broquet et al. 2017]. Important challenges of satellite measurements are that they are not as accurate as in-situ ones, having larger systematic errors, while the XCO<sub>2</sub> gradients in the column are typically 7-8 times smaller than in the boundary layer. Another difficulty of space-borne imagery with passive instruments is that they will only sample city XCO<sub>2</sub> plumes during clear sky conditions for geostationary satellites and with an additional constraint to observations at around mid-day for low-earth orbiting satellites.

The recent development of a robust portable ground-based FTIR (Fourier Transform InfraRed) spectrometer as described in Gisi et al. [2012] and Hase et al. [2015] (EM27/SUN, Bruker Optik, Germany) greatly facilitates the measurement of XCO<sub>2</sub> from the surface, with better accuracy than from space and with the possibility of continuous daytime observation during clear sky conditions. Typical compatibility (uncorrected bias) of the EM27/SUN retrievals of the different instruments in a local network is better than 0.01 % (i.e. ~ 0.04 ppm) after a careful calibration procedure and a harmonized processing scheme for all spectrometers [Frey et al. 2015]. The Collaborative Carbon Column Observing Network (COCCON) [Frey et al. 2018] intends to offer such a framework for operating the EM27/SUN. This type of spectrometer therefore represents a remarkable opportunity to document XCO<sub>2</sub> variability in cities as a direct way to estimate FFCO<sub>2</sub> [Hase et al. 2015] or in preparation of satellite missions.

When future low-Earth-orbit operational satellites with imaging passive spectrometers of suitable capabilities to invert FFCO<sub>2</sub> will sample different cities, this will likely be limited to clear

sky conditions and at a time of the day close to local noon. Increasing the density of the COCCON network stations around cities will allow to evaluate those XCO<sub>2</sub> measurements and to monitor XCO<sub>2</sub> during the early morning and afternoon periods which will not be sampled with low-earth orbit satellites. From geostationary orbit, which can also have other benefits, those time-periods can however be observed and could be compared to ground-based measurements [e.g. Butz et al., 2015, O'Brien et al. 2016].

This study focuses on the measurements of XCO<sub>2</sub> from ground based EM27/SUN spectrometers deployed within the Paris metropolitan area during a field campaign in the spring of 2015, and modelling results. This campaign can be seen as a demonstration of the COCCON network concept applied to the quantification of an urban FFCO<sub>2</sub> source. Several spectrometers were operated by different research groups, while closely following the common procedures suggested by Frey et al. [2015]. The paper is organised as follows. After the instrumental and modelling setup descriptions of section 2, the observations of the field campaign and the modelling results will be presented in section 3. Results are discussed in section 4 together with the study conclusions.

## **2 Methods and materials**

### **2.1 Description of study area and field campaign design**

During the COCCON field campaign (April 28th to May 13th, 2015) five portable FTIR spectrometers (EM27/SUN, Bruker Optik, Karlsruhe, Germany) were deployed in the Parisian region (administratively known as *Île-de-France*) and within the city of Paris. The campaign was conducted in early spring as the cloud cover is typically low in April and May and the time between sunrise and sunset is more than 14 hours.

The Paris metropolitan area houses over 12 million people, with about 2.2 million inhabiting the city of Paris. This urban region is the most densely populated in France with ~1000 inhabitants/km<sup>2</sup> and over 21000 inhabitants/km<sup>2</sup> for the city of Paris itself [INSEE 2016 - <https://www.insee.fr/fr/statistiques>]. The estimated CO<sub>2</sub> emissions from the metropolitan region are 39 Mt/year, according to the air quality association AIRPARIF (Association de surveillance de la qualité de l'air en Île-de-France), that monitors the airshed of Greater Paris. On-road traffic emissions, residential and the tertiary (i.e. commercial) sector are the main sources (accounting for over 75 %), and minor contributions from other sectors such as industrial sources and airports [<https://www.airparif.asso.fr/en/>, AIRPARIF 2016]. It was crucial to understand the spatial distribution of these CO<sub>2</sub> sources to optimally deploy the COCCON spectrometers. To this end a 1 km emission model for France by IER (Institut fuer Energiewirtschaft und Rationelle Energieanwendung, University of Stuttgart, Germany) was used as a starting point [Latoska 2009]. This emission inventory is based on the available activity data such as, e.g., traffic counts, housing statistics, or energy use, and the temporal

disaggregation was implemented according to Vogel et al. [2013]. In brief, the total emissions of the IER model were re-scaled to match the temporal factors for the different emission sectors according to known national temporal emission profiles.

To quantify the impact of urban emissions on  $\text{XCO}_2$ , the FTIR instruments were deployed along the dominant wind directions in this region in spring, i.e., southwesterly [Staufer et al 2016], in order to maximize the likelihood to capture upwind and downwind air masses (see Figure 1). The two southwesterly sites (GIF and RES) are located in a less densely populated area, where emissions are typically lower than in the city centre, where the station JUS is located. The data in Fig. 1 show that the densest FFCO<sub>2</sub> emission area extends northwards and eastwards. The two Northwesterly sites (PIS and MIT) were placed downwind of this area. All instruments were operated manually and typically started operations around 7-8 am local time from which they continuously observe  $\text{XCO}_2$  until 5-6 pm.

## **2.2 Instrumentation, calibration, and data processing**

The EM27/SUN is a portable FTIR spectrometer which has been described in detail in, e.g., Gisi et al. [2012] and Frey et al. [2015]. Here, only a short overview is given. The centre piece of the instrument is a Michelson interferometer which splits up the incoming solar radiation into two beams. After inserting a path difference between the beams, the partial beams are recombined. The modulated signal is detected by an InGaAs detector covering the spectral domain from 5000 to 11000  $\text{cm}^{-1}$  and is called an interferogram. As the EM27/SUN analyzes solar radiation, it can only operate in daylight sunny conditions. A Fourier transform of the interferogram generates the spectrum and a DC correction is applied to remove the background signal and only keep the AC signal (see Keppel-Aleks et al. [2007]). A numerical fitting procedure (PROFFIT code) [Schneider and Hase et al., 2009] then retrieves column abundances of the concentrations of the observed gases from the spectrum. The single-channel EM27/SUN is able to measure total columns of  $\text{O}_2$ ,  $\text{CO}_2$ ,  $\text{CH}_4$  and  $\text{H}_2\text{O}$ . The ratio over the observed  $\text{O}_2$  column, assumed to be known and constant, delivers the column-averaged trace gas concentrations of  $\text{XCO}_2$ ,  $\text{XCH}_4$  in  $\mu\text{mol} / \text{mol}$  dry air, with a temporal resolution of one minute.  $\text{XCO}_2$  is the dry air mole fraction of  $\text{CO}_2$ , defined as  $\text{XCO}_2 = \text{Column}[\text{CO}_2] / \text{Column}[\text{Dry Air}]$ . Applying the ratio over the observed oxygen ( $\text{O}_2$ ) column reduces the effect of various possible systematic errors; see Wunch et al. (2011).

In order to correctly quantify small differences in  $\text{XCO}_2$  columns between Paris city upstream and downstream locations, measurements were performed with the five FTIR instruments side by side before and after the campaign, as we expect small calibration differences between the different instruments due to slightly different alignment for each individual spectrometer. These differences are constant over time and can be easily accounted for by applying a calibration factor for each instrument. Previous studies showed that the instrument specific corrections

are well below 0.1 % for XCO<sub>2</sub> [Frey et al. 2015, Chen et al. 2016] and are stable for individual devices. The 1-sigma precision for XCO<sub>2</sub> is in the order of 0.01 % - 0.02 % (< 0.08 ppm) e. g. [Gisi et al. 2012, Chen et al. 2016, Hedelius et al. 2016, Klappenbach et al. 2015]. The calibration measurements for this campaign were performed in Karlsruhe w.r.t. the Total Carbon Column Observing Network (TCCON) [Wunch et al. 2011] spectrometer at the Karlsruhe Institute of Technology (KIT), Germany for 7 days before the Paris campaign between April 9<sup>th</sup> and 23<sup>rd</sup>, and after the campaign on May 18<sup>th</sup> until 21<sup>st</sup>.

Figure S1 (left panel) shows the XCO<sub>2</sub> time series of the calibration campaign, where small offsets between the instruments raw data are visible. As these offsets are constant over time, a calibration factor for each instrument can be easily applied; actually these are the calibration factors previously found for the Berlin campaign [Frey et al. 2015]. These factors are given in Table 1, where all EM27/SUN instruments are scaled to match instrument No. 1. The calibrated XCO<sub>2</sub> values for April 15<sup>th</sup> are shown in Fig. S1 None of the five instruments that participated in the Berlin campaign show any significant drift; in other words, the calibration factors found one year before were still applicable. This is a good demonstration of the instrument stability stated in section 2.2, especially as several instruments (Nos. 1, 3, 5) were used in another campaign in Northern Germany in the meantime. The EM27/SUN XCO<sub>2</sub> measurements can also be made traceable to the WMO international scale for in-situ measurements by comparison with measurements of a collocated TCCON spectrometer which are calibrated against in-situ standards by aircraft and aircore measurements [Wunch et al. 2010, Messerschmidt et al. 2012] performed using the WMO scale.

During the campaign and for the calibration measurements we recorded double-sided interferograms with 0.5 cm<sup>-1</sup> spectral resolution. Each measurement of 58 s duration consisted of 10 scans using a scanner velocity of 10 kHz. For precise timekeeping, we used GPS sensors for each spectrometer.

In-situ surface pressure data used for the analysis of the calibration measurements performed at KIT have been recorded at the co-located meteorological tall tower. During the campaign, a MHD-382SD data-logger recorded local pressure, temperature and relative humidity at each station. The analysis of the trace gases from the measured spectra for the calibration measurements has been performed as described by Frey et al. [2015]. For the campaign measurements we assume a common vertical pressure-temperature profile for all sites, provided by the model, so that the surface pressure at each spectrometer only differs due to different site altitudes. The 3-hourly temperature profile from the European Centre for Medium-Range Weather Forecasts (ECMWF) operational analyses interpolated for site JUS located in the centre of the array was used for the spectra analysis at all sites. The individual ground-pressure was derived from site altitudes and pressure measurements performed at each site.

Before and after the Paris campaign, side by side comparison measurements were performed with all 5 EM27/SUN spectrometers and the TCCON spectrometer operated in Karlsruhe at KIT. All spectrometers were placed on the top of the IMK office building North of Karlsruhe. The altitude is 133 m above sea level (a.s.l.), coordinates are 49.09° N and 8.43° E. The processing of the Paris raw observations (measured interferograms) were performed as described by Gisi et al. [2012] and Frey et al. [2015] for the Berlin campaign: spectra were generated applying a DC correction, a Norton-Beer medium apodization function and a spectral resampling of the sampling grid resulting from the FFT on a minimally sampled spectral grid. PROFFWD was used as the radiative transfer model and PROFFIT as the retrieval code.

### **2.3 Atmospheric transport modelling framework**

We used the chemistry transport model CHIMERE (Menut et al., 2013) to simulate CO<sub>2</sub> concentrations in the Paris area. More specifically, we used the CHIMERE configuration over which the inversion system of Bréon et al. [2015] and Staufer et al. [2016] was built to derive monthly to 6-hour mean estimates of the CO<sub>2</sub> Paris emissions. Its horizontal grid, and thus its domain and its spatial resolution, are illustrated in Figure S2. It has a 2 × 2 km<sup>2</sup> spatial resolution for the Paris region, and 2 × 10 km<sup>2</sup> and 10 × 10 km<sup>2</sup> spatial resolutions for the surroundings. It has 20 vertical hybrid pressure-sigma (terrain- following) layers that range from the surface to the mid-troposphere, up to 500 hPa. It is driven by operational meteorological analyses of the ECMWF Integrated Forecasting System, available at an approximately 15 × 15 km<sup>2</sup> spatial resolution and 3 h temporal resolution.

In this study the CO<sub>2</sub> simulations are based on a forward run over April 25<sup>th</sup> - May 12<sup>th</sup> 2015 with this model configuration; we do not assimilate atmospheric CO<sub>2</sub> data and so no inversion for surface fluxes was conducted. In the Paris area (the Île-de-France administrative region), hourly anthropogenic emissions are given by the IER inventory, see section 2.1. The anthropogenic emissions in the rest of the domain are prescribed from the EDGAR V4.2 database for the year 2010 at 0.1° resolution [Olivier and Janssens-Maenhout et al., 2012]. In the whole simulation domain, the natural fluxes (the Net Ecosystem Exchange: NEE) are prescribed using simulations of C-TESSEL, which is the land-surface component of the ECMWF forecasting system [Boussetta et al., 2013], at a 3 hourly and 15 × 15 km<sup>2</sup> resolution. Finally, the CO<sub>2</sub> boundary conditions at the lateral and top boundaries of the simulation domain and the simulation CO<sub>2</sub> initial conditions on April 25<sup>th</sup> 2015 are prescribed using the CO<sub>2</sub> forecast issued by the Copernicus Atmosphere Monitoring Service (CAMS, <http://atmosphere.copernicus.eu/>) at a ~15 km global resolution [Agustí-Panareda et al., 2014].

The CHIMERE transport model is used to simulate the XCO<sub>2</sub> data. However, since the model does not cover the atmosphere up to its top, the CO<sub>2</sub> fields from CHIMERE are complemented with that of the CAMS CO<sub>2</sub> forecasts from 500 hPa to the top of the atmosphere to derive total column concentrations. The derivation of modelled XCO<sub>2</sub> at the sites, involves obtaining a kernel-smoothed CO<sub>2</sub> profile of CHIMERE and CAMS and vertical integration of these smoothed profiles, weighted by the pressure at the horizontal location of the sites.

The parametrisation used to smooth modelled CO<sub>2</sub> profiles approximates the sensitivity of the EM27/sun CO<sub>2</sub> retrieval is a function of pressure and sun elevation. Between 1000 hPa and 480 hPa, a linear dependency of the instrument averaging kernels on solar zenith angle ( $\theta$ ) is assumed with boundary values following Frey et al. [2015]:

$$(1a) \quad k(480 \text{ hPa}) = 1.125$$

$$(1b) \quad k(1000 \text{ hPa}) = 1.0 + 0.45 s^3$$

where  $s = \theta/90^\circ$ .  $k$ . Approximate averaging kernels are obtained bylinear interpolation to the pressure levels of CHIMERE and CAMS, respectively. If  $p > 1000$  hPa,  $k$  is linearly extrapolated. Above 480 hPa ( $p < 480$  hPa), the averaging kernels can be approximated by

$$(2) \quad k(u, s) = 1.125 - 0.6 u^3 - 0.4 u s^3$$

where  $u$  is  $(480 \text{ hPa} - p) / 480$ . The kernel-smoothed CO<sub>2</sub> profile,  $CO_{2\_model}^s$ , is obtained by

$$(3) \quad CO_{2\_model}^s = \mathbf{K} CO_{2\_model} + (\mathbf{I} - \mathbf{K}) CO_2^a$$

where  $CO_{2\_model}$  is the modelled CO<sub>2</sub> profile by CHIMERE or CAMS,  $\mathbf{I}$  the identity matrix and  $\mathbf{K}$  is a diagonal matrix containing the averaging kernels  $k$ . The a priori CO<sub>2</sub> profile,  $CO_2^a$ , is provided by the Whole Atmosphere Community Climate Model (WACCM) model (version 6) and interpolated to the pressure levels of CHIMERE and CAMS.  $CO_{2\_model}^s$  is the appropriate CO<sub>2</sub> profile to calculate modelled XCO<sub>2</sub> at the location of the sites.

For a given site, the simulated XCO<sub>2</sub> data are thus computed from the vertical profile of this site as:

$$(3) \quad XCO_{2\_CHIMERE} = \frac{1}{P_{surf}} \int_{P_{surf}}^{P_{top\_CHIM}} CO_{2\_CHIM}^s dp + \int_{P_{top\_CHIM}}^{P=0mbar} CO_{2\_CAMs}^s dp$$

where  $p_{surf}$  is the surface pressure,  $p_{top\_CHIM} = 500$  hPa the pressure corresponding to the top boundary of the CHIMERE model, and  $CO_{2\_CHIM}^s$  and  $CO_{2\_CAMS}^s$  are the smoothed  $CO_2$  concentrations of CHIMERE and CAMS respectively. For comparison we also calculated  $XCO_2$  at a lower spatial resolution with the CAMS data alone as:

$$(4) \quad XCO_{2\_CAMS} = \int_{P_{surf}}^{P=0mbar} CO_{2\_CAMS}^s dP$$

### 3 Results and discussion

#### 3.1 Observations

##### 3.1.1 Meteorological conditions and data coverage/instrument performance.

During the measurement campaign (April 28<sup>th</sup> until May 13<sup>th</sup>, 2015), meteorological conditions were a major limitation for the availability of  $XCO_2$  observations. Useful EM27/SUN measurements require direct sunlight and low wind speeds typically yield higher local  $XCO_2$ . Most of the time during the campaign conditions were partly cloudy and turbid, and so successful measurements at high solar zenith angle (SZA) were rare. Therefore, the data coverage between April 28<sup>th</sup> and May 3<sup>rd</sup> is limited (see Table 2). As is typical for spring periods in Paris, the temperature and the wind direction vary and display less synoptic variations than in winter. The dominant wind directions were mostly northeasterly at the beginning of the campaign and mostly southeasterly during the second half of the campaign. We find that the wind speeds during daytime nearly always surpass  $3 \text{ m s}^{-1}$ , which has been identified by Breon et al. [2015] and Stauffer et al. [2016] as the cut-off wind speed above which the atmospheric transport model CHIMERE performs best in modelling  $CO_2$  concentration gradients in the mixed layer.

Despite some periods with unfavourable conditions, more than 10,000 spectra were retrieved among the five deployed instruments. The quality of the spectra for each day was rated according to the overall data availability and consistent with Hase et al. (2015). The best measurement conditions prevailed for the period between May 7<sup>th</sup> and May 12<sup>th</sup>.

##### 3.1.2 Observations of $XCO_2$ in Paris

The observed  $XCO_2$  in the Paris region for all sites (10415 observations) ranges from 397.27 to 404.66 ppm with a mean of 401.26 ppm (a median of 401.15 ppm). The strong atmospheric variability of  $XCO_2$  across Paris and within the campaign period is reflected in the standard deviation of 1.04 ppm for 1-minute averages. We find that all sites exhibit very similar diurnal behaviours with a clear decrease of  $XCO_2$  during daytime and a noticeable day-to-day variability as seen in Figure 2. This is to be expected as they are all subject to very similar atmospheric transport in the boundary layer height and to similar large-scale influences, i.e.,

surrounding with stronger natural fluxes or air mass exchange with other regions at synoptic time scales. However, observed XCO<sub>2</sub> concentrations at the downwind sites for our network remain clearly higher from sites that are upwind of Paris (see Figure 2). The shifting dominant wind conditions also explain why the site RES and GIF are lowest in the beginning of the campaign and higher on May 12<sup>th</sup> and 13<sup>th</sup> after meteorological conditions changed. This indicates that the influence of urban emissions is detectable with this network configuration under favourable meteorological conditions. By comparing the different daily variations in Fig. 3, it is apparent that the day-to-day variations observed at the two southwesterly (typically upwind) sites GIF and RES are approximately 1 ppm, with both sites exhibiting similar diurnal variations throughout the campaign period. This can be expected as their close vicinity would suggest that they are sensitive to emissions from similar areas and to concentrations of air masses arriving from the southwest.

The typical decrease in XCO<sub>2</sub> found over the course of a day is about 2 to 3 ppm. This decrease could be driven by (natural) sinks of CO<sub>2</sub>, which can be expected to be very strong as our campaign took place after the start of the growing season in Europe for most of southern and central Europe [Roetzer and Chmielewski 2001].

The observations at the site located in Paris (JUS) displays similarly low day-to-day variations and a clear decrease in XCO<sub>2</sub> over the course of the day. The latter feature indicates that even in the dense city centre, XCO<sub>2</sub> is primarily representative of a large footprint like in other areas of the globe [Keppel-Aleks 2011] and supports the findings of Belikov et al. (2017) concerning the footprints for the Paris and Orleans TCCON sites. Thus, our total column observations are less critically affected by local emissions than in-situ measurements [Breon et al. 2015, Ammoura et al. 2016]. It is also apparent that the decrease in XCO<sub>2</sub> (the slope) during the afternoon for April 28<sup>th</sup> and 29<sup>th</sup> as well as May 7<sup>th</sup> and 10<sup>th</sup> is noticeably smaller than at other days during this campaign. As XCO<sub>2</sub> is not sensitive to vertical mixing, this has to be caused by different CO<sub>2</sub> sources and sinks acting upon the total column arriving at JUS.

The two (typically downwind) sites PIS and MIT northeast of Paris show a markedly larger day-to-day spread in their general XCO<sub>2</sub> levels as well as strongly changing slopes for the diurnal XCO<sub>2</sub> decrease. For these sites the exact wind direction is critical as they can be downwind of the city centre that has a much higher emission density or less dense suburbs (see Fig. 1).

### **3.1.3 Gradients in observed XCO<sub>2</sub>**

In order to focus more on the impact of local emissions on atmospheric conditions and less on that of CO<sub>2</sub> fluxes from outside of our urban domain in our analysis of XCO<sub>2</sub>, we choose to study the spatial gradients ( $\Delta$ ) between different sites. Fundamentally, this approach assumes that regional and large-scale fluxes have a similar impact on XCO<sub>2</sub> for the sites within our

network, due to the close proximity of sites and the smoothing of remote emission signals due to atmospheric transport by the time the air-mass arrives in our domain. Ideal conditions were sampled during May 7<sup>th</sup>, with predominantly southwesterly winds, and on May 10<sup>th</sup> with southerly winds. We can see in Fig. 4 that all sites were, on average, elevated compared to RES, chosen as reference here as it was upwind of Paris during those days. The hodographs for both days also indicate that the wind fields were consistent across Paris (see Figure S3). The observations from GIF showed only minimal differences with RES, while the rest of the sites (PIS, JUS and MIT) had  $\Delta$  values of 1 to 1.5 ppm. During southwesterly winds, MIT is downwind of the densest part of the Paris urban area, and JUS is impacted by emissions of neighborhoods to the southwest. The site of PIS is still noticeably influenced by the city centre but, as can be seen in Fig. 1, we likely do not catch the plume of the most intense emissions but rather from the suburbs. On May 10<sup>th</sup>, with its dominant southerly winds, the situation was markedly different. While GIF was still only slightly elevated, the XCO<sub>2</sub> enhancement at MIT was significantly lower and quite similar to JUS for large parts of the day. The highest  $\Delta$ XCO<sub>2</sub> can be observed at PIS, again typically ranging from 1 to 1.5 ppm. As seen in Fig. 1, PIS is then directly downwind of the densest emission area, while MIT is only exposed to CO<sub>2</sub> emissions from the eastern outskirts of Paris.

It is also important to note that the impact of the local biosphere that is assumed to cause the strong decrease in XCO<sub>2</sub> during the day is not seen on both days for these spatial gradients. For a more comprehensive interpretation of these observations the use of a transport model (as described in section 2.3) is necessary.

## **3.2 Modelling**

### **3.2.1 Model performance**

Before interpreting the modelled XCO<sub>2</sub> we need to evaluate the performance of the chosen atmospheric transport model framework as described in section 2.3. Comparing it to meteorological observations (wind speed and wind direction) at GIF, we find that CHIMERE predicts these variables well throughout the duration of the campaign (see Figure S4). Changes in wind speed direction and speed are reproduced with a slight overestimation at low wind-speeds (>1m/s). Besides the meteorological forcing, the model performance can also be expected to depend on the chosen model resolution. Therefore, we compared XCO<sub>2</sub> at JUS calculated based on the coarser resolution atmospheric transport and flux framework CAMS (15 km), and the higher resolution emission modelling input for the framework based on CHIMERE (2 km) for the inner domain and on CAMS boundary conditions (see Fig. S2). We find that the coarser model displays similar inter-daily variations, but that the high-resolution model modifies the modelling results on shorter time-scales. We find that the afternoon XCO<sub>2</sub> decreases are often more pronounced in CHIMERE. Only the high-resolution will be

considered and referred to in the following. The impact of using different flux maps (fossil fuel CO<sub>2</sub>) on the modelled XCO<sub>2</sub> can unfortunately not be explicitly investigated here as only one high-resolution (1 km) emission product available for fossil fuel CO<sub>2</sub> was available for this study region (see section 2.3) and other global emission products are usually not intended for urban-scale studies.

### 3.2.2 Modelled XCO<sub>2</sub> and its components

The modelled XCO<sub>2</sub> for the five sites (Fig. 5) co-evolves over the period of the campaign with occurrences of significant differences. This was already seen with the measurements, but the model allows looking at the full time series. The model reveals clear daily cycles of XCO<sub>2</sub>, with an accumulation during night-time and a decrease during daytime. Despite a good general agreement of modelled XCO<sub>2</sub> at all sites for, e.g., the timing of daily minima and their synoptic changes, differences in XCO<sub>2</sub> are observed between the sites for many days. Typically the northeasterly sites (PIS, MIT) show an enhancement in modelled XCO<sub>2</sub> compared to the southwesterly sites (GIF, RES).

To understand the synoptic and diurnal variations of the modelled XCO<sub>2</sub>, we analyzed the contribution of different sources (and sinks) of CO<sub>2</sub>, namely the net ecosystem exchange (NEE), the fossil fuel CO<sub>2</sub> emissions (FFCO<sub>2</sub>), and the boundary conditions (BC), i.e., the variations of CO<sub>2</sub> not caused by fluxes within our domain (the example of JUS is given in Fig. 6). The day-to-day variability of modelled XCO<sub>2</sub> is dominated by changing boundary conditions and coincides with synoptic weather changes. As the CO<sub>2</sub> emitted from the different sources is transported in the model as independent tracers, the strong daily decrease in XCO<sub>2</sub> can be directly linked to NEE, which leads to a decrease of ~1 ppm (but up to 4 ppm) during the day, but can also cause positive enhancements during nighttime driven by biogenic respiration. The XCO<sub>2</sub> from fossil fuel emissions causes significant enhancements compared to the background, but is often compensated by NEE. During short periods, fossil fuel emissions can however lead to enhancements of up to 4 ppm.

### 3.2.3 Modelled $\Delta$ XCO<sub>2</sub> gradients and its components

To be able to assess the impact of local sources and reduce the influence of NEE and BC on the modelled signals, we analyse the XCO<sub>2</sub> gradient (i.e. station-to-station difference) with RES being taken as reference. In Fig. 7 we compare  $\Delta$ , in the top panel, and its components, i.e. fossil fuel CO<sub>2</sub>, biogenic CO<sub>2</sub> and CO<sub>2</sub> transported across the boundary of the domain (boundary conditions: BC), along a south-north direction. For the modelled  $\Delta$  we can see that MIT shows a positive value during the campaign period whenever the predominant wind direction was southwesterly. We also find that  $\Delta$  between JUS and RES was both negative and positive during the campaign, and predominantly negative between MIT and JUS. When

split into FFCO<sub>2</sub>, BC and NEE components, we can clearly see that the total  $\Delta$  is dominated by FF causing XCO<sub>2</sub> offsets of up to 4 ppm, but more typically 1 ppm gradients are observed. Gradients can also change rapidly (within a few hours) if the wind direction changes, for example on May 1<sup>st</sup> and May 12<sup>th</sup>. This highlights the fact that, during such conditions, we cannot assume a simple upwind-downwind interpretation of our sites. As expected, the contributions from BC and NEE are generally greatly reduced when analysing  $\Delta$ XCO<sub>2</sub>. The most important impact of NEE on the XCO<sub>2</sub> gradients of -1ppm and +1ppm can be seen on May 8<sup>th</sup> and May 11<sup>th</sup>, respectively. This means that, despite greatly reducing the impact of NEE on average, the contribution of NEE cannot be fully ignored. BC is an overall negligible contribution to  $\Delta$ XCO<sub>2</sub>, even though it reaches -0.4 ppm on May 11<sup>th</sup>.

### **3.3 Model data and observations comparison**

#### **3.3.1 XCO<sub>2</sub>**

A comparison of modelled and observed XCO<sub>2</sub> is of course limited to the relatively short periods when observations are available. Over these periods we can see a general issue in reproducing the general XCO<sub>2</sub> for each day in the model as observed XCO<sub>2</sub> is significantly lower revealing a fairly stable bias between 1 to 2 ppm. As our CO<sub>2</sub> boundary conditions were from a forecast product, this is not unexpected, as already small issues in estimating carbon uptake (or emissions) at the European scale can have such an impact on the boundary conditions. However, we observe that the main features, like daily cycles and synoptic changes of the modelled and observed XCO<sub>2</sub> are comparable as seen in Figure 8. The daytime variations are well reproduced by the model and the general relative concentrations between sites are preserved, e.g., the highest values for XCO<sub>2</sub> at MIT are on May 9<sup>th</sup> and highest XCO<sub>2</sub> for PIS are later on May 10<sup>th</sup> and May 11<sup>th</sup>. We also see that the timing of the daily minima is not fully covered in the observed data as it typically happens after sunset and cessation of biosphere uptake. To reduce the impact of uncertainties of the boundary conditions on our analysis a gradient approach was tested.

#### **3.3.2 $\Delta$ XCO<sub>2</sub>**

Due to the prevailing southeasterly wind conditions, we can compare XCO<sub>2</sub> at the typical downwind sites (PIS, MIT) relative to the mostly upwind sites (RES, GIF) and expect elevated XCO<sub>2</sub> downwind. Furthermore, we can expect to see negative gradients for opposing wind conditions, i.e. northwesterly. For other wind conditions, the concentration difference is not determined by emissions between the station pairs, but rather by the areas upwind of the sites, (see Figure 1). We find that the model versus observed  $\Delta$ XCO<sub>2</sub> of PIS relative to RES generally falls along the 1:1 line with a slope of  $1.07 \pm 0.09$  with a Pearson's R of 0.8. Negative  $\Delta$ XCO<sub>2</sub>

values, seen in Fig. 9, are associated with meteorological conditions when winds come from northerly directions, i.e., the roles of normal upwind and downwind sites are reversed. For wind perpendicular to the direct line of sight for (PIS, RES) the concentration enhancements are small and harder to interpret. The gradient of  $XCO_2$  MIT relative to RES has a significantly lower range for modelled  $XCO_2$  while the observed range of  $XCO_2$  is similar to PIS. The slope of observed to modelled  $\Delta XCO_2$  for upwind-downwind (or downwind-upwind conditions) is  $1.72 \pm 0.06$  with a Pearson's R of 0.96. This points to a significant underestimation of the impact of urban sources on the MIT-RES gradient, which is especially visible in the more negative  $\Delta XCO_2$  during northerly wind conditions. This could indicate that the spatial distribution of our emissions prior should be improved, i.e., emissions in the eastern outskirts/suburbs are likely underestimated in the IER emissions model. The low modelled  $\Delta XCO_2$  could also be due to overestimated horizontal dispersion in the model, which seems less likely. Again the model does not predict concentration differences well for perpendicular wind conditions. When comparing the mean modelled daily cycle of the days with south-westerly wind conditions and when observations exist with the mean diurnal cycle for all days within the field campaign period when MIT and PIS can be considered downwind of RES, we find that the days with observations do not significantly differ from those without observations (see Fig. 10). An investigation of typical diurnal variations of modelled  $\Delta XCO_2$  can only be performed to a limited degree with the observational data available for suitable wind conditions. Within the large uncertainties, the modelled and observed  $\Delta XCO_2$  agree throughout the day. When analysing the modelled  $\Delta XCO_2$  components we also find that the observed daytime increases of  $\Delta XCO_2$  are driven by  $CO_2$  added by urban FF  $CO_2$  burning and that the impact of FF is significantly higher at PIS (up to 1 ppm) than at MIT site (0.5 ppm) in the model, when both sites are downwind of Parisian emissions. Our observations indicate that both sites have strong diurnal variations. Given that the most important biogenic sinks, in our domain, can be expected to be found in the rural parts surrounding Paris we would expect the biogenic contribution to be similar at both sites (as predicted by the model). This would further point towards, that the impact of FF emissions on the MIT site is larger than predicted by our modelling framework. Different  $\Delta XCO_2$  diurnal variations can be found for other upwind-downwind site pairs, but they are all systematically driven by the locally-added  $CO_2$  from FFCO<sub>2</sub>.

## 5 Conclusion and Outlook

For the two-week field campaign we demonstrated the ability of a network of five EM27/SUN spectrometers, placed in the outskirts of Paris, to track the  $XCO_2$  changes due to the urban plume of the city. However, we also found that  $XCO_2$  cannot be simply interpreted in the context of local emissions as, even in such a densely populated area,  $XCO_2$  is still significantly

influenced by natural CO<sub>2</sub> uptake during the growing season. Understanding the area  
 influencing XCO<sub>2</sub> and/or the use of suitable atmospheric transport models seems  
 indispensable to correctly interpret atmospheric XCO<sub>2</sub> variations. Using a gradient approach,  
 i.e., analysing the difference between XCO<sub>2</sub> measured at upwind and downwind stations,  
 greatly reduced the impact of CO<sub>2</sub> boundary condition, that reflect fluxes outside the domain  
 and biogenic fluxes within the domain. Overall, the XCO<sub>2</sub> variability modelled using our  
 ECMWF-CHIMERE system with IER (1 x 1 km<sup>2</sup>) emissions data was found to be comparable  
 with the observed variability and diurnal evolution of XCO<sub>2</sub>, despite a higher background for  
 modelled XCO<sub>2</sub>. Our modelling framework, run at a 2 x 2 km<sup>2</sup> resolution over Paris also  
 predicts that biogenic fluxes and boundary conditions (i.e. the influence of CO<sub>2</sub> being  
 transported into our domain) have only very small impact on ΔXCO<sub>2</sub> only noticeably impacting  
 it during a few situations, specifically when meteorological conditions changes made the  
 concept of ‘upwind’ and ‘downwind’ not applicable. When comparing modelled and measured  
 ΔXCO<sub>2</sub> we find strong correlations (Pearson’s R) of 0.8 and 0.96 for PIS-RES and MIT-RES,  
 respectively. The offset between model and observations also diminished for ΔXCO<sub>2</sub> and the  
 slope found between observed and modeled PIS-RES gradient is statistically in accordance  
 with a 1:1 relationship (1.07±0.09). However, the slope of the MIT-RES XCO<sub>2</sub> gradient of  
 1.72±0.06 suggests that the emission model could potentially be improved, as it seems  
 unlikely that the general atmospheric transport in the model is the key issue as both site pairs  
 would be subject to very similar winds. Another potential source of error that needs to be  
 investigated is if such an underestimation of ΔXCO<sub>2</sub> could be caused by the limited model  
 resolution.. It also seems rather likely that a 2x2km<sup>2</sup> model would cause a general spreading  
 of point source emissions and not systematically underestimate emissions impacts from less  
 densely populated, parts of Île-de-France. The data also confirm previous results by models  
 that XCO<sub>2</sub> gradients caused by a megacity do not exceed 2 ppm, which supports the previous  
 requirement for satellite observations of less than 1 ppm precision on individual soundings,  
 and biases lower than 0.5 ppm (Ciais et al. 2015). The gradients are mainly caused by the  
 transport of FFCO<sub>2</sub> emissions but, interestingly, during specific episodes, a noticeable  
 contribution comes from biogenic fluxes, suggesting that these fluxes cannot always be  
 neglected even when using gradients.

Unfortunately, the duration of the campaign was relatively short, so that an in-depth analysis  
 of mean daily cycles or the impact of ambient conditions (traffic conditions, temperature, solar  
 insolation, etc.) on the observed gradient and underlying fluxes could not be investigated here.  
 Hence, future studies in Paris and elsewhere should aim to perform longer-term observations  
 during different seasons, which will allow better understanding changes in biogenic and  
 anthropogenic CO<sub>2</sub> fluxes. A remotely-controllable shelter for the EM27/SUN instrument is

currently under development [Heinle and Chen, 2017]. This will considerably facilitate the establishment of permanent spectrometer arrays around cities and other sources of interest. Nevertheless, our study already indicates that such observations of urban XCO<sub>2</sub> and ΔXCO<sub>2</sub> contain original information to understand local sources and sinks and that the modelling framework used here is a step forward to support their detailed interpretation in the future. An improved model will also be able to adjust or better model the background conditions and potentially use this type of observations to estimate local CO<sub>2</sub> fluxes using a Bayesian inversion scheme similar to the existing system based on in-situ observations for Paris [Stauffer et al. 2016].

We expect that the previous successful collaboration in the framework of the Paris campaign will mark the permanent implementation of COCCON as a common framework for a French-Canadian-German collaboration on the EM27/SUN instrument. The acquisition of additional spectrometers is planned by several partners.

#### **Author contribution**

FRV, MF, FH, IXR, MKS, PCh, PJ, YVT, CJ, TB, QT and JO, supported the field campaign and contributed data to this study.

MF, FH, FRV, JS, GB and PCi planned the fieldwork and modelling activities for this study. JS, GB, FC, and FRV performed the CHIMERE modelling, provided modelling data input and/or analysed the output data.

MF, FH and FRV processed and analysed the EM27Sun data.

FRV, MF, JS, FH and PCi wrote sections of the manuscript and created figures and tables.

All authors reviewed, edited and approved the manuscript.

#### **Acknowledgement**

All authors would like to thank the two anonymous reviewers for their comments that helped to significantly improve this manuscript. ECCO would like to thank Ray Nasser (CRD) and Yves Rochon (AQRD) for their internal review. The authors from LSCE acknowledge the support of the SATINV group of Frederic Chevallier. The authors from KIT acknowledge support from the Helmholtz Research Infrastructure ACROSS. The authors from LISA acknowledge support from the OSU-EFLUVE (Observatoire des Sciences de l'Univers-Enveloppes Fluides de la Ville à l'Exobiologie).

#### **References**

Agustí-Panareda, A., Massart, S., Chevallier, F., Bousetta, S., Balsamo, G., Beljaars, A., Ciais, P., Deutscher, N.M., Engelen, R., Jones, L. and Kivi, R., 2014. Forecasting global atmospheric CO<sub>2</sub>. *Atmospheric Chemistry and Physics*, 14(21), pp.11959-11983.

586 AIRPARIF, 2016. Inventaire régional des émissions en Île-de-France Année de référence 2012 –  
 587 éléments synthétiques, Edition Mai 2016, Paris, France. Last access Dec. 14th, 2017, available at:  
 588 [https://www.airparif.asso.fr/\\_pdf/publications/inventaire-emissions-idf-2012-150121.pdf](https://www.airparif.asso.fr/_pdf/publications/inventaire-emissions-idf-2012-150121.pdf)  
 589 Ammoura, L., Xueref-Remy, I., Vogel, F., Gros, V., Baudic, A., Bonsang, B., Delmotte, M., Té, Y. and  
 590 Chevallier, F., 2016. Exploiting stagnant conditions to derive robust emission ratio estimates for CO<sub>2</sub>,  
 591 CO and volatile organic compounds in Paris. *Atmospheric Chemistry and Physics*, 16(24), pp.15653-  
 592 15664.  
 593 Belikov, D., Maksyutov, S., Ganshin, A., Zhuravlev, R., Deutscher, N.M., Wunch, D., Feist, D.G.,  
 594 Morino, I., Parker, R.J., Strong, K. and Yoshida, Y., 2017. Study of the footprints of short-term  
 595 variation in XCO<sub>2</sub> observed by TCCON sites using NIES and FLEXPART atmospheric transport  
 596 models.  
 597 Bréon, F.M., Broquet, G., Puygrenier, V., Chevallier, F., Xueref-Remy, I., Ramonet, M., Dieudonné, E.,  
 598 Lopez, M., Schmidt, M., Perrussel, O. and Ciais, P., 2015. An attempt at estimating Paris area CO<sub>2</sub>  
 599 emissions from atmospheric concentration measurements. *Atmospheric Chemistry and Physics*, 15(4),  
 600 pp.1707-1724. <https://doi.org/10.5194/acp-15-1707-2015>, 2015.  
 601 Broquet, G., Bréon, F.M., Renault, E., Buchwitz, M., Reuter, M., Bovensmann, H., Chevallier, F., Wu,  
 602 L. and Ciais, P., 2018. The potential of satellite spectro-imagery for monitoring CO<sub>2</sub> emissions from  
 603 large cities. *Atmospheric Measurement Techniques*, 11(2), pp.681-708.  
 604 Boussetta, S., Balsamo, G., Beljaars, A., Panareda, A.A., Calvet, J.C., Jacobs, C., Hurk, B., Viterbo,  
 605 P., Lafont, S., Dutra, E. and Jarlan, L., 2013. Natural land carbon dioxide exchanges in the ECMWF  
 606 Integrated Forecasting System: Implementation and offline validation. *Journal of Geophysical*  
 607 *Research: Atmospheres*, 118(12), pp.5923-5946.  
 608 Butz, A., Orphal, J., Checa-Garcia, R., Friedl-Vallon, F., von Clarmann, T., Bovensmann, H.,  
 609 Hasekamp, O., Landgraf, H., Knigge, T., Weise, D., Sqalli-Houssini, O., and D. Kemper, *Geostationary*  
 610 *Emission Explorer for Europe (G3E): mission concept and initial performance assessment*, *Atmos.*  
 611 *Meas. Tech.*, 8, 4719-4734, 2015  
 612 Chen, J., Viatte, C., Hedelius, J. K., Jones, T., Franklin, J. E., Parker, H., Gottlieb, E. W., Wennberg, P.  
 613 O., Dubey, M. K., and Wofsy, S. C., 2016. Differential column measurements using compact solar-  
 614 tracking spectrometers, *Atmos. Chem. Phys.*, 16, 8479-8498, [https://doi.org/10.5194/acp-16-8479-](https://doi.org/10.5194/acp-16-8479-2016)  
 615 2016, 2016.  
 616 Ciais, P., Crisp, D., Denier van der Gon, H., Engelen, R., Heimann, M., Janssens-Maenhout, G.,  
 617 Rayner, P. and Scholze, M., 2015. Towards a European Operational Observing System to Monitor  
 618 Fossil CO<sub>2</sub> Emissions. Final Report from the Expert Group, European Commission, October 2015.  
 619 Available at [http://edgar.jrc.ec.europa.eu/news\\_docs/CO2\\_report\\_22-10-2015.pdf](http://edgar.jrc.ec.europa.eu/news_docs/CO2_report_22-10-2015.pdf) Accessed February  
 620 6th, 2018  
 621 Dhakal, S., 2009. Urban energy use and carbon emissions from cities in China and policy implications,  
 622 *Energy Policy* 37:4208-4219  
 623 Frey, M., F. Hase, T. Blumenstock, J. Groß, M. Kiel, G. Mengistu Tsidu, K. Schäfer, M. Kumar Sha, and  
 624 J. Orphal, 2015. Calibration and instrumental line shape characterization of a set of portable FTIR  
 625 spectrometers for detecting greenhouse gas emissions, *Atmos. Meas. Tech.*, 8, 3047-3057,  
 626 doi:10.5194/amt-8-3047-2015

627 Frey, M., Sha, M.K., Hase, F., Kiel, M., Blumenstock, T., Harig, G., Surawicz, G., Deutscher, N.M.,  
628 Shiomi, K., Franklin, J., Bösch, H., Chen, J., Grutter, M., Ohyama, H., Sun, Y., Butz, A., Mengistu Tsidu,  
629 G., Ene, D., Wunch, D., Song, C.Z., Garcia, O., Ramonet, M., Vogel, F., and J. Orphal, Building the  
630 COllaborative Carbon Column Observing Network (COCCON): Long term stability and ensemble  
631 performance of the EM27/SUN Fourier transform spectrometer, *Atmos. Meas. Tech.* Diss, submitted,  
632 2018

633 Gisi, M., F. Hase, S. Dohe, T. Blumenstock, A. Simon, and A. Keens, 2012. XCO<sub>2</sub>-measurements with  
634 a tabletop FTS using solar absorption spectroscopy, *Atmos. Meas. Tech.*, 5, 2969-2980,  
635 doi:10.5194/amt-5-2969-2012

636 Hase, F., M. Frey, T. Blumenstock, J. Groß, M. Kiel, R. Kohlhepp, G. Mengistu Tsidu, K. Schäfer, M. K.  
637 Sha, and J. Orphal, 2015. Application of portable FTIR spectrometers for detecting greenhouse gas  
638 emissions of the major city Berlin, *Atmos. Meas. Tech.*, 8, 3059-3068, doi:10.5194/amt-8-3059-2015

639 Hase, F., M. Frey, M. Kiel, T. Blumenstock, R. Harig, A. Keens, and J. Orphal, 2016. Addition of a  
640 channel for XCO observations to a portable FTIR spectrometer for greenhouse gas measurements,  
641 *Atmos. Meas. Tech.*, 9, 2303-2313, doi:10.5194/amt-9-2303-2016

642 Hedelius, J. K., Viatte, C., Wunch, D., Roehl, C. M., Toon, G. C., Chen, J., Jones, T., Wofsy, S. C.,  
643 Franklin, J. E., Parker, H., Dubey, M. K., and Wennberg, P. O., 2016. Assessment of errors and biases  
644 in retrievals of XCO<sub>2</sub>, XCH<sub>4</sub>, XCO, and XN<sub>2</sub>O from a 0.5 cm<sup>-1</sup> resolution solar-viewing spectrometer, *Atmos.*  
645 *Meas. Tech.*, 9, 3527-3546, <https://doi.org/10.5194/amt-9-3527-2016>

646 Heinle, L. and Chen, J., 2017 in review. Automated Enclosure and Protection System for Compact  
647 Solar-Tracking Spectrometers, *Atmos. Meas. Tech. Discuss.*, <https://doi.org/10.5194/amt-2017-292>

648 IEA, International Energy Agency, 2008, World Energy Outlook, IEA Publications, Paris, France ISBN:  
649 978926404560-6

650 IPCC-WG1, Climate Change 2013: The Physical Science Basis. Contribution of Working Group I to the  
651 Fifth Assessment Report of the Intergovernmental Panel on Climate Change [Stocker, T.F., D. Qin, G.-  
652 K. Plattner, M. Tignor, S.K. Allen, J. Boschung, A. Nauels, Y. Xia, V. Bex and P.M. Midgley (eds.)].  
653 Cambridge University Press, Cambridge, United Kingdom and New York, NY, USA, 1535 pp

654 IPCC-WG3, Climate Change 2014: Mitigation of Climate Change. Contribution of Working Group III to  
655 the Fifth Assessment Report of the Intergovernmental Panel on Climate Change [Edenhofer, O., R.  
656 Pichs-Madruga, Y. Sokona, E. Farahani, S. Kadner, K. Seyboth, A. Adler, I. Baum, S. Brunner, P.  
657 Eickemeier, B. Kriemann, J. Savolainen, S. Schlömer, C. von Stechow, T. Zwickel and J.C. Minx (eds.)].  
658 Cambridge University Press, Cambridge, United Kingdom and New York, NY, USA

659 Janardanan, R., S. Maksyutov, T. Oda, M. Saito, J. W. Kaiser, A. Ganshin, A. Stohl, T. Matsunaga, Y.  
660 Yoshida, and T. Yokota (2016), Comparing GOSAT observations of localized CO<sub>2</sub> enhancements by  
661 large emitters with inventory-based estimates, *Geophys. Res. Lett.*, 43, 3486–3493,  
662 doi:10.1002/2016GL067843.

663 Jones, N., 2013, Troubling milestone for CO<sub>2</sub>. *Nature Geoscience* 6, no. 8, 589-589.

664 Keppel-Aleks, G., Toon, G.C., Wennberg, P.O. and Deutscher, N.M., 2007. Reducing the impact of  
665 source brightness fluctuations on spectra obtained by Fourier-transform spectrometry. *Applied optics*,  
666 46(21), pp.4774-4779.

667 Keppel-Aleks, G., P. O. Wennberg, and T. Schneider (2011), Sources of variations in total column  
 668 carbon dioxide, *Atmospheric Chemistry and Physics*, 11(8), 3581-3593, doi:10.5194/acp-11-3581-2011  
 669 Klappenbach, F., Bertleff, M., Kostinek, J., Hase, F., Blumenstock, T., Agusti-Panareda, A., Razinge,  
 670 M., and Butz, A., 2015. Accurate mobile remote sensing of XCO<sub>2</sub> and XCH<sub>4</sub> latitudinal transects from  
 671 aboard a research vessel, *Atmos. Meas. Tech.*, 8, 5023-5038, <https://doi.org/10.5194/amt-8-5023-2015>  
 672 Kort, E. A., C. Frankenberg, C. E. Miller, and T. Oda (2012), Space-based observations of megacity  
 673 carbon dioxide, *Geophys. Res. Lett.*, 39, L17806, doi:10.1029/2012GL052738.  
 674 Lauvaux, T., Miles, N.L., Deng, A., Richardson, S.J., Cambaliza, M.O., Davis, K.J., Gaudet, B., Gurney,  
 675 K.R., Huang, J., O'Keefe, D. and Song, Y., 2016. High-resolution atmospheric inversion of urban CO<sub>2</sub>  
 676 emissions during the dormant season of the Indianapolis Flux Experiment (INFLUX). *Journal of*  
 677 *Geophysical Research: Atmospheres*, 121(10), pp.5213-5236.  
 678 Latoska, A., 2009. Erstellung eines räumlich hoch aufgelösten Emissionsinventar von Luftschadstoffen  
 679 am Beispiel von Frankreich im Jahr 2005, Master's thesis, Institut für Energiewirtschaft und Rationelle  
 680 Energieanwendung, Universität Stuttgart, Stuttgart, Germany  
 681 Levin, I., Hammer, S., Eichmann, E. and Vogel, F.R., 2011. Verification of greenhouse gas emission  
 682 reductions: the prospect of atmospheric monitoring in polluted areas. *Philosophical Transactions of the*  
 683 *Royal Society of London A: Mathematical, Physical and Engineering Sciences*, 369(1943), pp.1906-  
 684 1924.  
 685 Messerschmidt, J., Geibel, M. C., Blumenstock, T., Chen, H., Deutscher, N. M., Engel, A., Feist, D. G.,  
 686 Gerbig, C., Gisi, M., Hase, F., Katrynski, K., Kolle, O., Lavrič, J. V., Notholt, J., Palm, M., Ramonet, M.,  
 687 Rettinger, M., Schmidt, M., Sussmann, R., Toon, G. C., Truong, F., Warneke, T., Wennberg, P. O.,  
 688 Wunch, D., and Xueref-Remy, I., 2011. Calibration of TCCON column-averaged CO<sub>2</sub>: the first aircraft  
 689 campaign over European TCCON sites, *Atmos. Chem. Phys.*, 11, 10765-10777,  
 690 <https://doi.org/10.5194/acp-11-10765-2011>  
 691 Mitchell, L.E., Lin, J.C., Bowling, D.R., Pataki, D.E., Strong, C., Schauer, A.J., Bares, R., Bush, S.E.,  
 692 Stephens, B.B., Mendoza, D. and Mallia, D., 2018. Long-term urban carbon dioxide observations reveal  
 693 spatial and temporal dynamics related to urban characteristics and growth. *Proceedings of the National*  
 694 *Academy of Sciences*, 115(12), pp.2912-2917.  
 695 Nassar, R., Hill, T.G., McLinden, C.A., Wunch, D., Jones, D.B.A. and D. Crisp, 2017. Quantifying CO<sub>2</sub>  
 696 emissions from individual power plants from space, *JGR*, 44, 19, 10045-1053.  
 697 Nassar, R., Napier-Linton, L., Gurney, K.R., Andres, R.J., Oda, T., Vogel, F.R. and Deng, F., 2013.  
 698 Improving the temporal and spatial distribution of CO<sub>2</sub> emissions from global fossil fuel emission data  
 699 sets. *Journal of Geophysical Research: Atmospheres*, 118(2), pp.917-933.  
 700 O'Brien, D.M., Polonsky, I.N., Utembe, S.R. and Rayner, P.J., 2016. Potential of a geostationary  
 701 geoCARB mission to estimate surface emissions of CO<sub>2</sub>, CH<sub>4</sub> and CO in a polluted urban environment:  
 702 case study Shanghai. *Atmospheric Measurement Techniques*, 9(9), p.4633.  
 703 Olivier, J. and G. Janssens-Maenhout, CO<sub>2</sub> Emissions from Fuel Combustion -- 2012 Edition, IEA CO<sub>2</sub>  
 704 report 2012, Part III, Greenhouse-Gas Emissions, ISBN 978-92-64-17475-7  
 705 Rötzer, T. and F-M. Chmielewski. 2001. Phenological maps of Europe., *Climate research* 18.3, 249-  
 706 257.

707 Schwandner, F.M., Gunson, M.R., Miller, C.E., Carn, S.A., Eldering, A., Krings, T., Verhulst, K.R.,  
 708 Schimel, D.S., Nguyen, H.M., Crisp, D. and O'dell, C.W., 2017. Spaceborne detection of localized  
 709 carbon dioxide sources. *Science*, 358(6360), p.eaam5782.  
 710 Schneider, M. and Hase, F.: Ground-based FTIR water vapour profile analyses, *Atmos. Meas. Tech.*,  
 711 2, 609–619, doi:10.5194/amt-2-609-2009, 2009.  
 712 Staufer, J., Broquet, G., Bréon, F.M., Puygrenier, V., Chevallier, F., Xueref-Rémy, I., Dieudonné, E.,  
 713 Lopez, M., Schmidt, M., Ramonet, M. and Perrussel, O., 2016. The first 1-year-long estimate of the  
 714 Paris region fossil fuel CO<sub>2</sub> emissions based on atmospheric inversion. *Atmospheric Chemistry and*  
 715 *Physics*, 16(22), pp.14703-14726.  
 716 Strong, C., Stwertka, C., Bowling, D.R., Stephens, B.B. and Ehleringer, J.R., 2011. Urban carbon  
 717 dioxide cycles within the Salt Lake Valley: A multiple-box model validated by observations. *Journal of*  
 718 *Geophysical Research: Atmospheres*, 116(D15).  
 719 Turnbull, J.C., Sweeney, C., Karion, A., Newberger, T., Lehman, S.J., Tans, P.P., Davis, K.J., Lauvaux,  
 720 T., Miles, N.L., Richardson, S.J. and Cambaliza, M.O., 2015. Toward quantification and source sector  
 721 identification of fossil fuel CO<sub>2</sub> emissions from an urban area: Results from the INFLUX experiment.  
 722 *Journal of Geophysical Research: Atmospheres*, 120(1), pp.292-312.  
 723 Vogel, F.R., Ishizawa, M., Chan, E., Chan, D., Hammer, S., Levin, I. and Worthy, D.E.J., 2012. Regional  
 724 non-CO<sub>2</sub> greenhouse gas fluxes inferred from atmospheric measurements in Ontario, Canada. *Journal*  
 725 *of Integrative Environmental Sciences*, 9(sup1), pp.41-55.  
 726 Vogel, F.R., Thiruchittampalam, B., Theloke, J., Kretschmer, R., Gerbig, C., Hammer, S. and Levin, I.,  
 727 2013. Can we evaluate a fine-grained emission model using high-resolution atmospheric transport  
 728 modelling and regional fossil fuel CO<sub>2</sub> observations?. *Tellus B: Chemical and Physical Meteorology*,  
 729 65(1), p.18681.  
 730 Wunch, D., Toon, G.C., Blavier, J.F.L., Washenfelder, R.A., Notholt, J., Connor, B.J., Griffith, D.W.T.,  
 731 Sherlock, V. and Wennberg, P.O., 2011. The total carbon column observing network, *Philos. T. Roy.*  
 732 *Soc. A*, 369, 2087–2112.  
 733 Wunch, D., Toon, C., Wennberg, O., Wofsy, C., Stephens, B., Fischer, L., Uchino, O., Abshire, B.,  
 734 Bernath, P., Biraud, C. and Blavier, F., 2010. Calibration of the total carbon column observing network  
 735 using aircraft profile data. *Atmospheric Measurement Techniques*, 3(5), pp.1351-1362.  
 736 Xueref-Remy, I., Dieudonné, E., Vuillemin, C., Lopez, M., Lac, C., Schmidt, M., Delmotte, M., Chevallier,  
 737 F., Ravetta, F., Perrussel, O., Ciais, P., Bréon, F.-M., Broquet, G., Ramonet, M., Spain, T. G., and  
 738 Ampe, C.: Diurnal, synoptic and seasonal variability of atmospheric CO<sub>2</sub> in the Paris megacity area,  
 739 *Atmospheric Chemistry and Physics*, 18(5), pp.3335-3362.

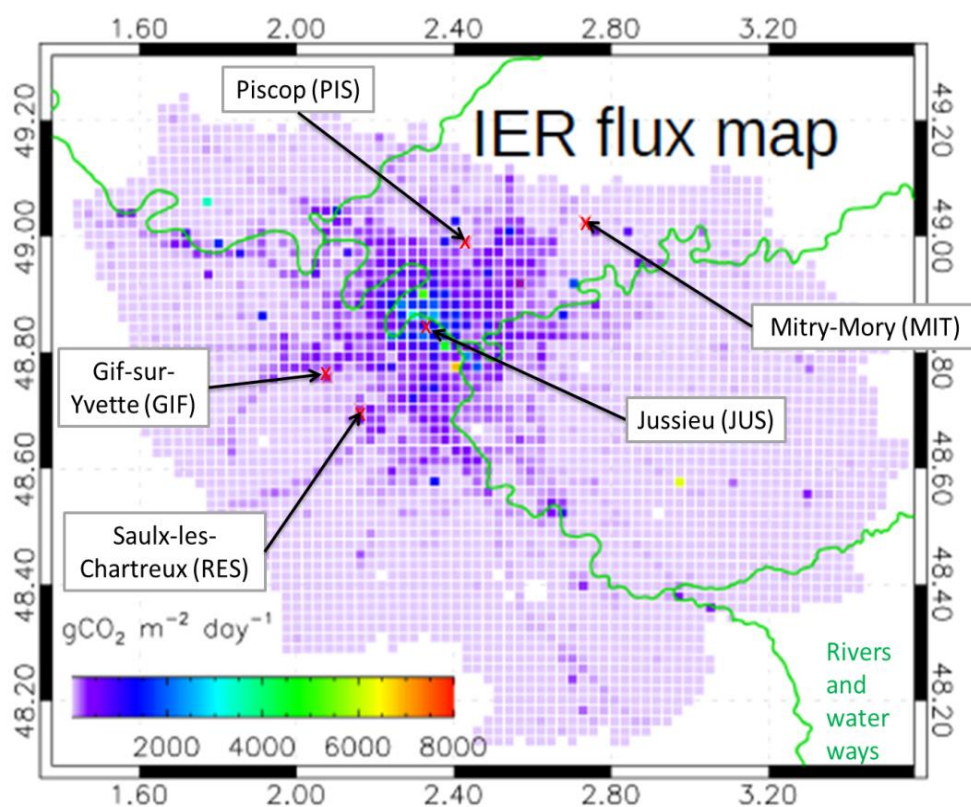


**Figure 1. CO<sub>2</sub> emissions in the Île-de-France region according to the IER emission inventory. Measurement sites are indicated by red crosses.**

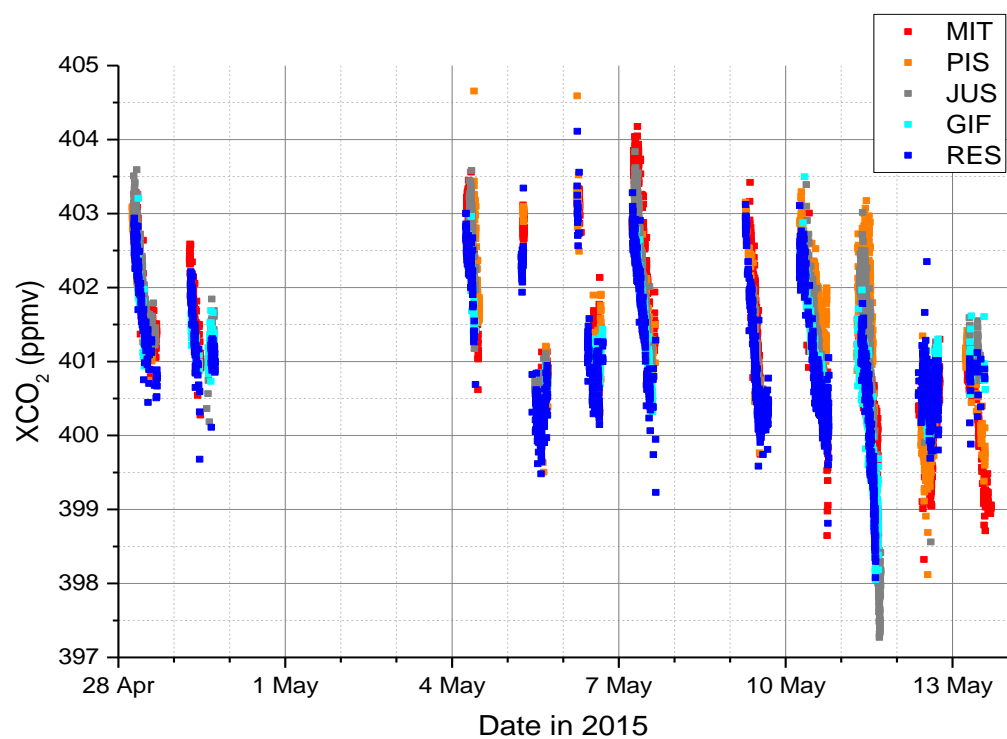


**Figure 2. Time series of observed XCO<sub>2</sub> in the Parisian region for all five sites (all valid data of 1 minute averages).**

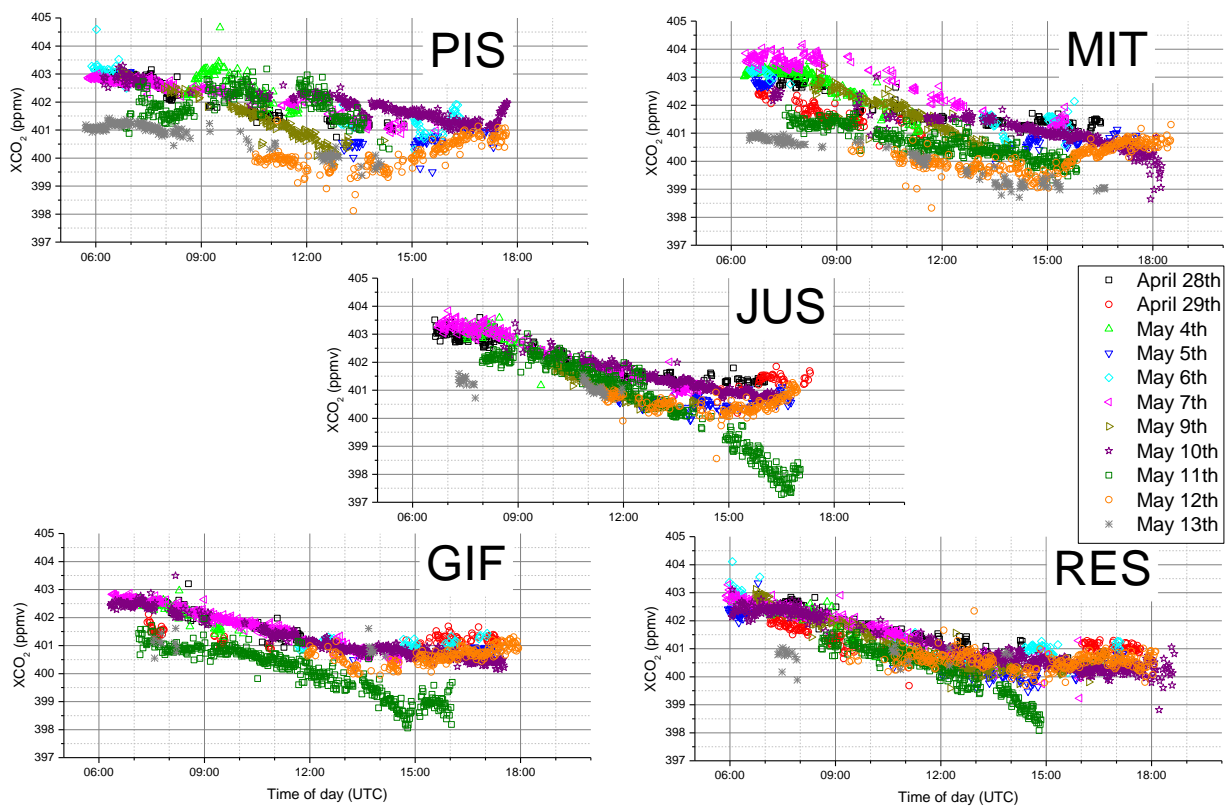


**Figure 3. Time series of observed  $XCO_2$  in the Parisian region sorted by station.**

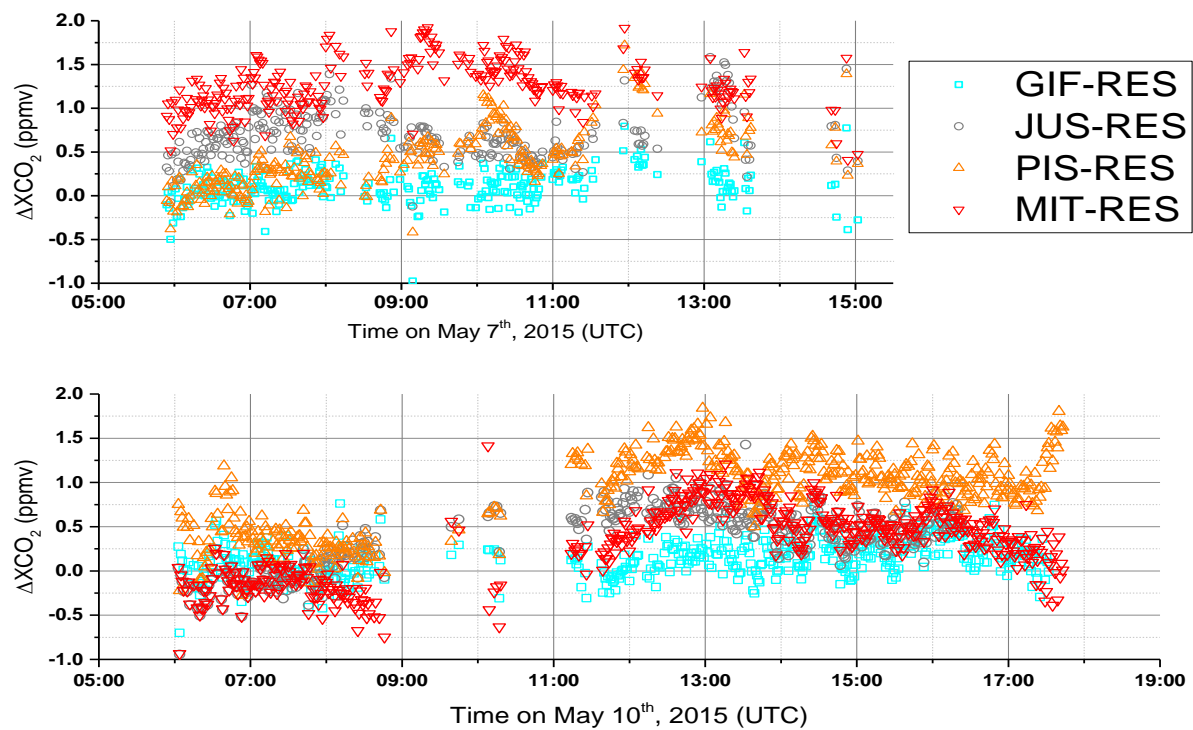
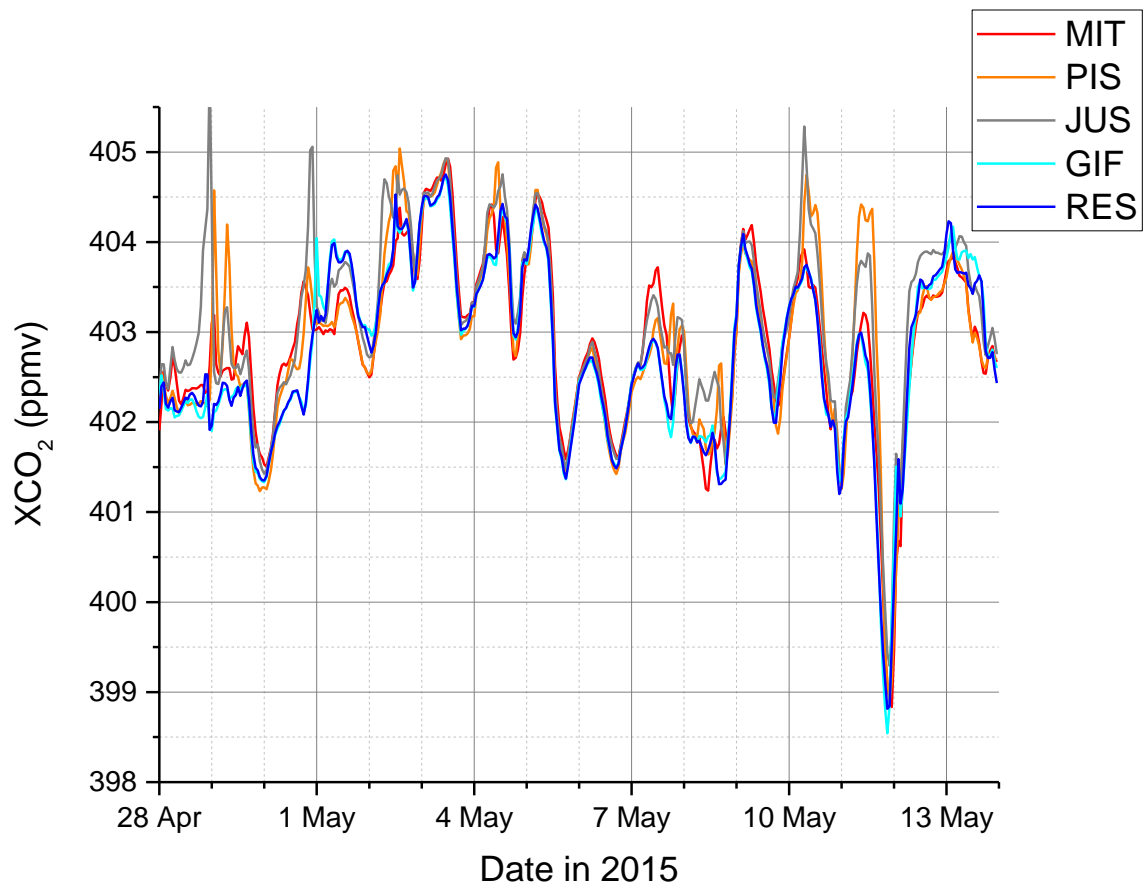


**Figure 4. Observed spatial gradients of XCO<sub>2</sub> for May 7<sup>th</sup> (southwesterly winds) and May 10<sup>th</sup> (southerly winds).**



751  
752 **Figure 5. Modelled XCO<sub>2</sub> for all stations.**

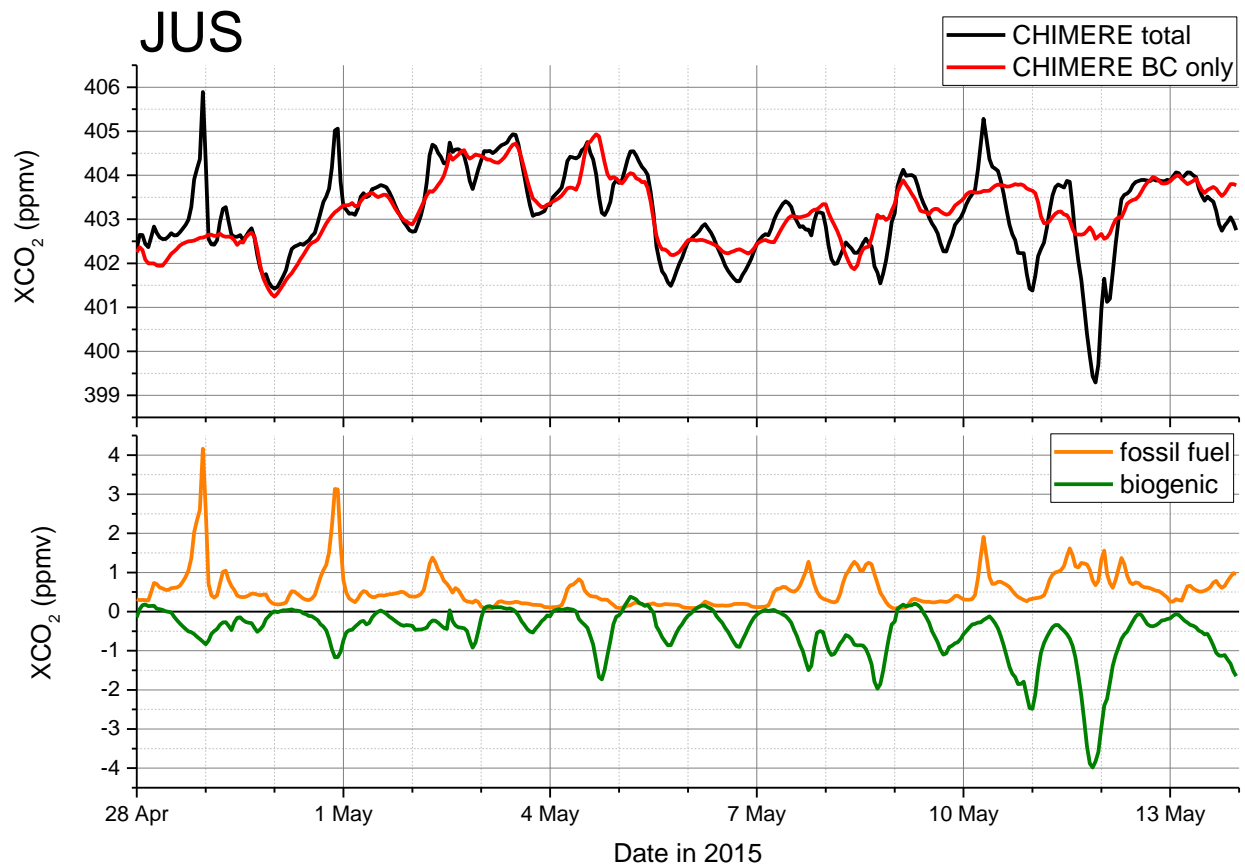


**Figure 6: Time series of  $XCO_2$  and related fluxes for JUS. The top panel provides a comparison of modelled total  $XCO_2$  and  $XCO_2$  variations due to changes in boundary conditions (BC only). The lower panel shows the contribution of the different flux components, namely fossil fuel  $CO_2$  emissions and biogenic fluxes.**

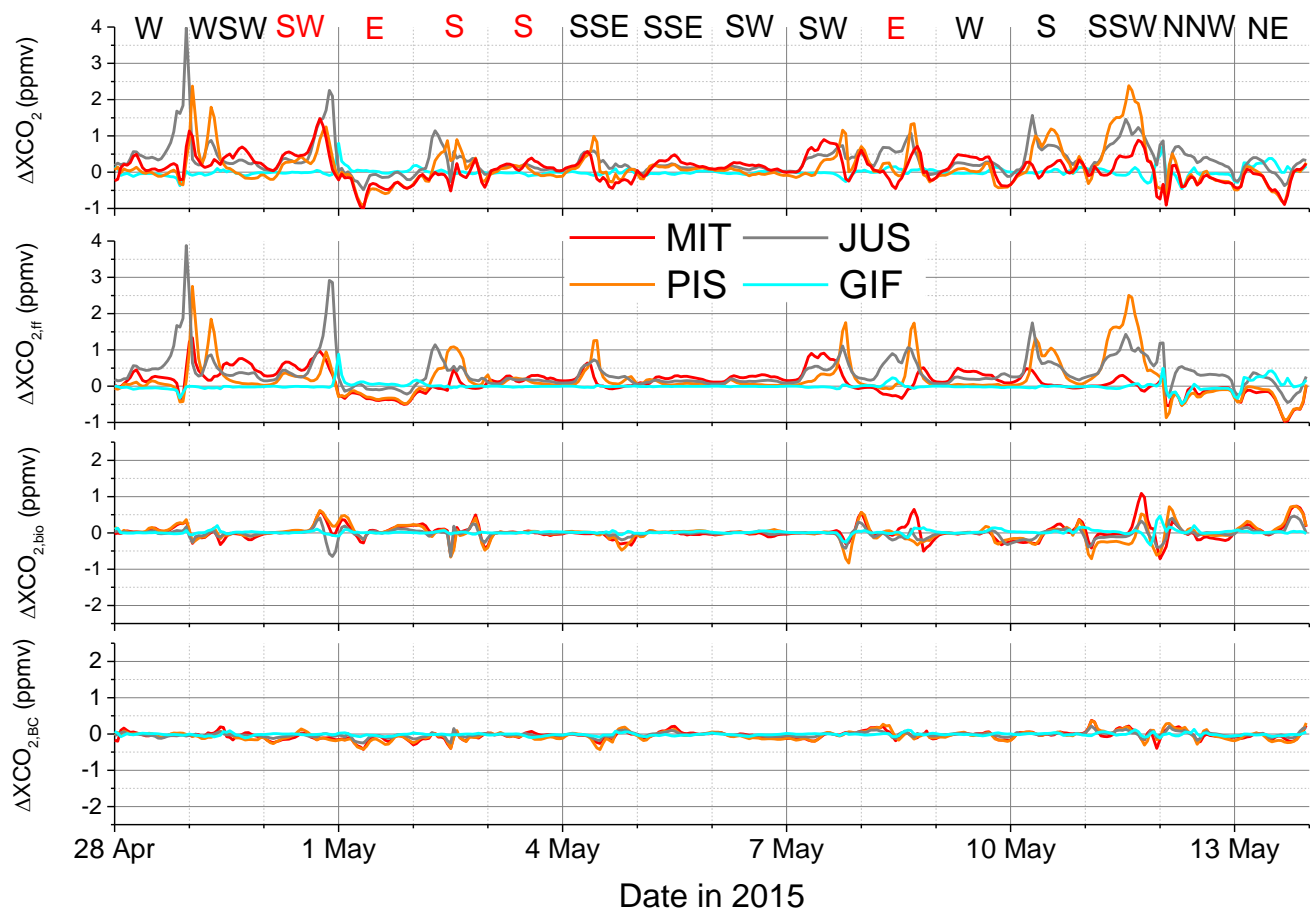


**Figure 7. Modelled  $XCO_2$  gradients for each station relative to RES are given in the top panel with its contributing components in the panels below. Total  $\Delta XCO_2$  (top), the fossil fuel contribution  $\Delta XCO_{2,ff}$  (second from top), the biogenic contribution  $\Delta XCO_{2,bio}$  (third from top) and the influence of the boundary conditions,  $\Delta XCO_{2,BC}$  (bottom). The dominant wind conditions for each day given at the top of the figure and days without observations due to precipitation are in red.**

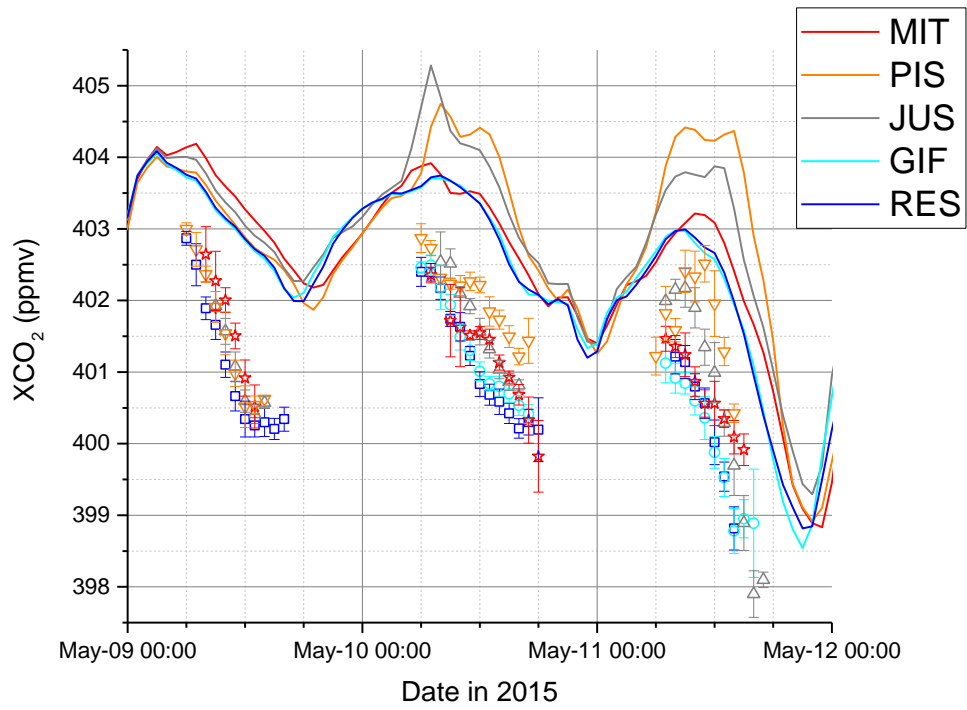


**Figure 8. Comparison of modelled (solid lines) and observed hourly averaged XCO<sub>2</sub> (symbols) with standard deviations as error bars.**

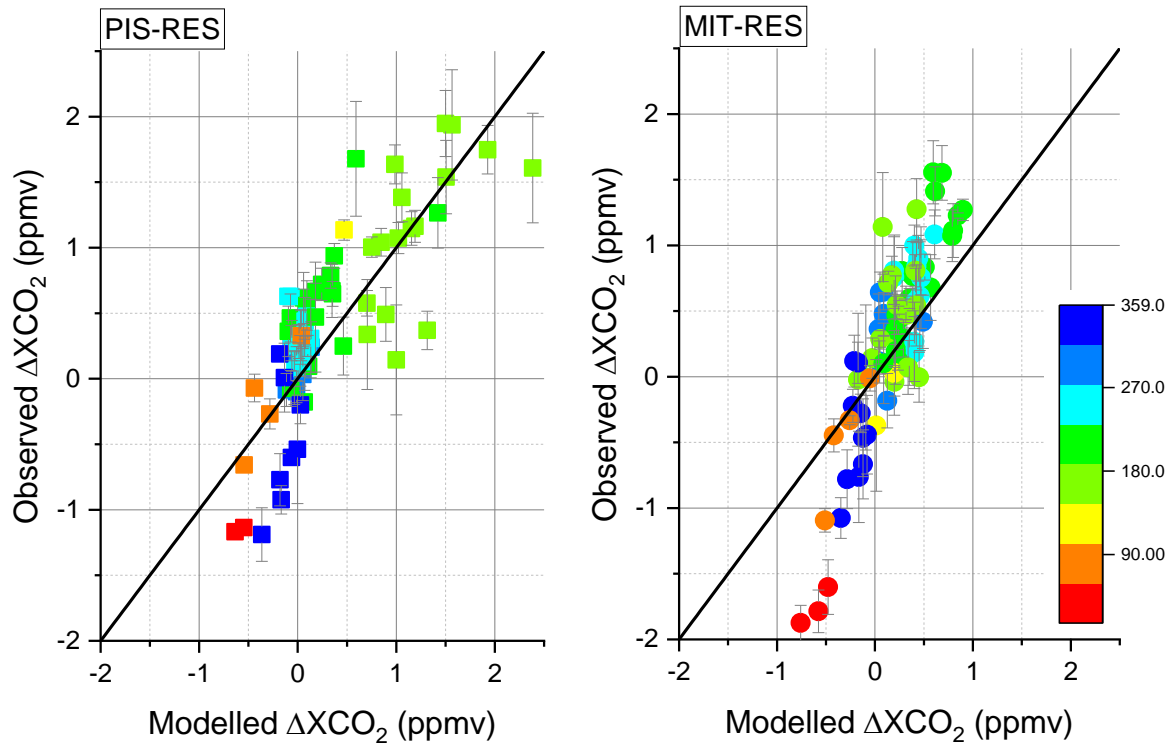


**Figure 9. Comparison of modelled and observed hourly averaged  $\Delta XCO_2$  for gradients between PIS and RES (left) and MIT and RES (right), with standard deviations of the minute values of the hourly mean as vertical bars and the points color coded by wind direction from 0 to 359 degrees.**

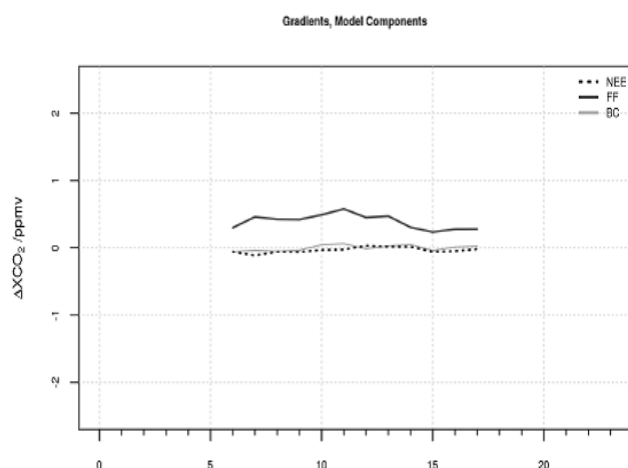
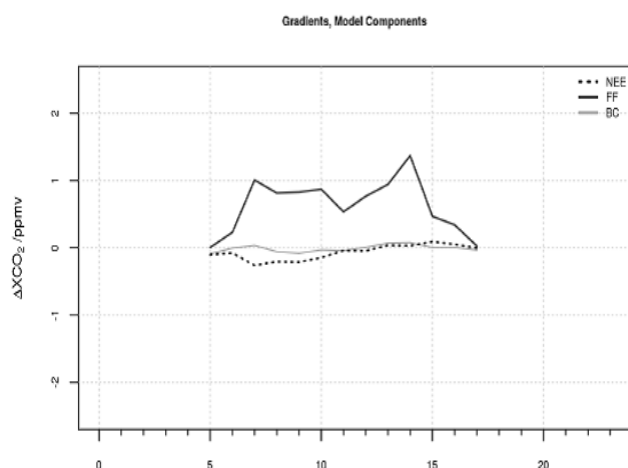
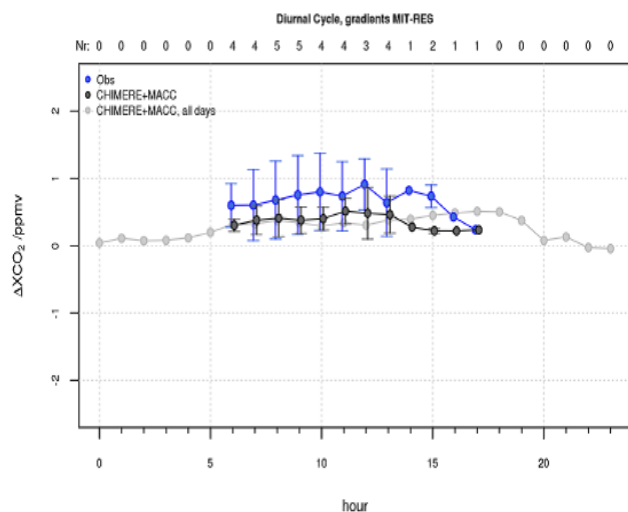
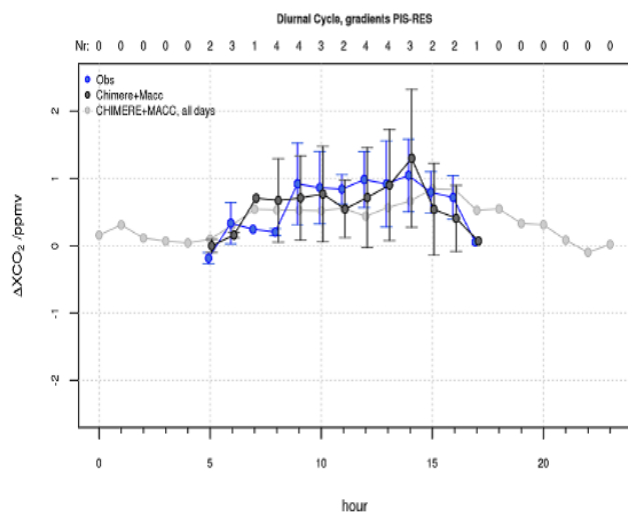


**Figure 10. Comparison of modelled (black) and observed mean daily cycle (blue) of hourly averaged  $\Delta XCO_2$  of PIS (top left) and of MIT (top right) during the campaign when RES can be considered as upwind site. Labels on top of the upper figures denote the number of days contributing to the mean. The mean daily cycle for all days within the campaign period when PIS and MIT are downwind of RES is given in light grey. The modelled contribution of different  $CO_2$  sources/sinks to the mean daily cycle for days with observations for the two sites is given in the bottom panels.**

Instrument	XCO <sub>2</sub> factor Berlin	XCO <sub>2</sub> factor before Paris	XCO <sub>2</sub> factor after Paris
1	1.0000 (0.0003)	1.0000 (0.0003)	1.0000 (0.0003)
2	0.9992 (0.0003)	0.9991 (0.0003)	0.9992 (0.0003)
3	1.0002 (0.0003)	1.0001 (0.0004)	1.0000 (0.0005)
4	0.9999 (0.0003)	1.0000 (0.0004)	1.0000 (0.0004)
5	0.9996 (0.0003)	0.9995 (0.0003)	0.9995 (0.0003)

Table 1. Normalisation factors for the five EM27/SUN instruments derived during measurements before and after the Paris field campaign. Values in parentheses are standard deviations. Measurements of instrument 1 were arbitrarily chosen as reference from which the others were scaled. The calibration factors from a previous field campaign in Berlin [Hase et al. 2015] are also shown. Calibration factors between the two field campaigns agree well within 0.02 % (~0.08 ppm) for all instruments.

Date	No. of observations					Quality	Wind speed (ms <sup>-1</sup> )	Wind direction
	MIT	GIF	PIS	RES	JUS			
28 Apr 2015 (Tu)	179	102	178	199	234	++	4	W
29 Apr 2015 (We)	110	124	0	161	53	+	5	SW-W
04 Mai 2015 (Mo)	194	85	96	163	83	+	6	S-SE
05 Mai 2015 (Tu)	77	27	85	185	92	+	8	S-SW
06 Mai 2015 (We)	81	88	87	139	0	+	8	SW
07 Mai 2015 (Th)	169	313	252	286	238	+++	3	SW
09 Mai 2015 (Sa)	179	0	181	289	149	++	6	W
10 Mai 2015 (Su)	325	478	362	542	282	++++	3	S
11 Mai 2015 (Mo)	410	431	251	298	413	++++	3	SSW
12 Mai 2015 (Tu)	324	222	230	326	203	+++	4	NNW
13 Mai 2015 (We)	159	18	182	28	56	+	4	NE

**Table 2. Summary of all measurement days with the number of observations at each of the sites, Mitry Mory (MIT) , Gif Sur Yvette (GIF), Piscop (PIS), Saulx-les-Chartreux (RES), Jussieu (JUS), the overall quality ranking of each day according to the number of available observations and temporal coverage (with classification from poor to great: +, ++, +++, ++++), and the ground-level wind speed and direction.**